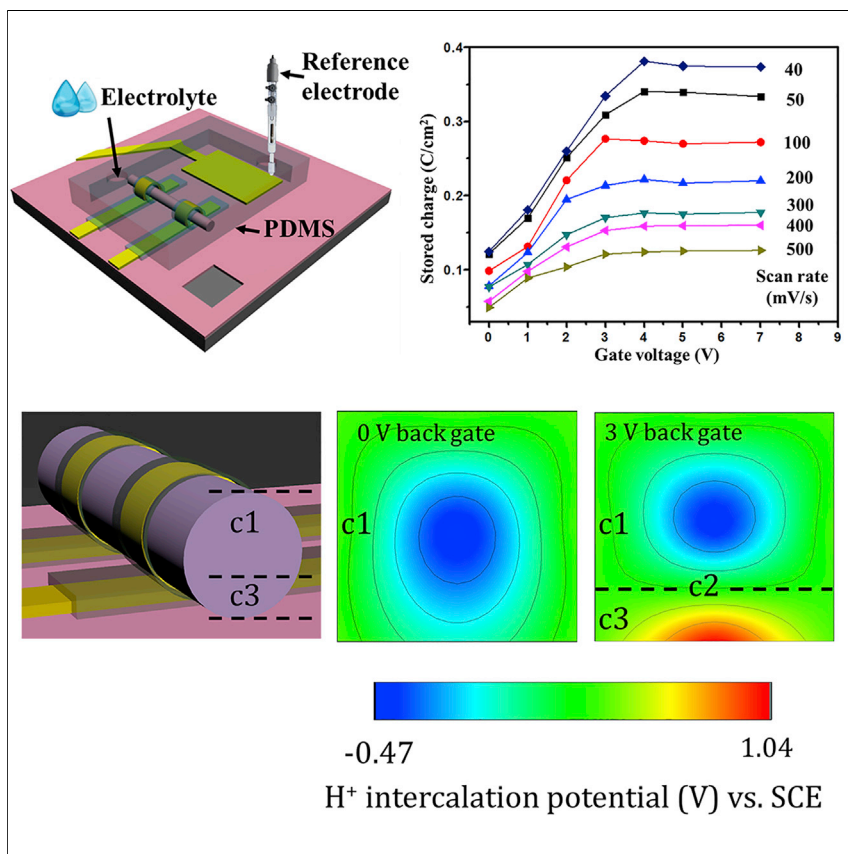


Article

Quadrupling the stored charge by extending the accessible density of states



Mengyu Yan, Peiyao Wang, Xuelei Pan, ..., Bruce Dunn, Jihui Yang, Liqiang Mai

mlq518@whut.edu.cn

Highlights

A 3-fold-enhanced stored charge under the field effect

The external electric field results in an extended accessible density of states

This field-effect-enhanced stored charge is applicable to redox reactions

Both energy-storage devices and billions of transistors have been integrated into tiny chips. Here, we demonstrated a boosted stored charge when the on-chip energy-storage devices meet with the transistors.



Article

Quadrupling the stored charge by extending the accessible density of states

Mengyu Yan,^{1,2,7} Peiyao Wang,^{1,3,7} Xuelel Pan,^{1,7} Qiulong Wei,¹ Chunhua Han,¹ Jefferson Zhe Liu,³ Yunlong Zhao,¹ Kangning Zhao,¹ Bruce Dunn,⁴ Jihui Yang,² and Liqiang Mai^{1,5,6,8,*}

SUMMARY

Nanosized energy storage, energy harvesting, and functional devices are the three key components for integrated self-power systems. Here, we report on nanoscale electrochemical devices with a nearly 3-fold-enhanced stored charge under the field effect. We demonstrated the field-effect transistor can not only work as a functional component in nanodevices but also serve as an amplifier for the nanosized energy-storage blocks. This unusual increase in energy storage is attributed to having a wide range of accessible electronic density of states (EDOS), and, hence, redox reactions are occurring within the nanowire and not being confined to the surface. Initial results with MoS₂ suggest that this field-effect-modulated energy-storage mechanism may also apply to many other redox-active materials. Our work demonstrates the novel application of the field effect in energy-storage devices as a universal strategy to improve ion diffusion, which can greatly enhance the charge storage ability of nanoscale devices.

INTRODUCTION

Nanoscale devices, such as intracellular recording sensors, electron devices, solar cells, thermoelectric conversion devices, and nanogenerators,^{1,2} show promise as fundamental building blocks in maintenance-free implantable biosensors.^{3–5} Traditionally, an integrated device contains three key components: energy-harvesting, energy-storage, and functional components (e.g., sensors, data transmitters, and data controllers). An energy-storage device can store discrete energy resources harvested by a solar cell, nanogenerator, or thermoelectric conversion device and then power the sensor and electronic device continuously. Thus, the development of nanoscale energy-storage devices is meaningful and important as an indispensable component in integrated maintenance-free devices.

Field effects are widely used for nanoscale electronic devices, such as in transistors for logic circuits and amplifiers,^{6–10} in field-induced electronic phase transitions^{11,12} and in the modulation of the liquid/solid interface for liquid-gated interfacial superconductivity.^{13,14} Although the use of magnetic field in conjunction with electrochemical energy-storage devices has shown some intriguing effects, it necessitates magnetic constituents in the devices, hence, limiting its application.^{15–17} To the best of our knowledge, the electrical field effects have not been integrated into any electrochemical energy-storage device. Although electrochemical energy-storage devices involve a change in electrical properties when charge transfer occurs,^{18,19} it is highly interesting to explore whether modulation of the electronic density of states (EDOS) is able to influence the energy-storage processes via the

The bigger picture

Nanosized energy-storage devices play an essential role in maintenance-free microprocessors and nanoscale energy-harvesting/sensing technologies. In this study, we proved that the field-effect transistor, which is the core component in microprocessors, can also serve as an amplifier for the nanosized energy-storage devices. A 3-fold-enhanced stored charge is achieved under the field effect, paving the way for the high-performance nanosized self-power system.

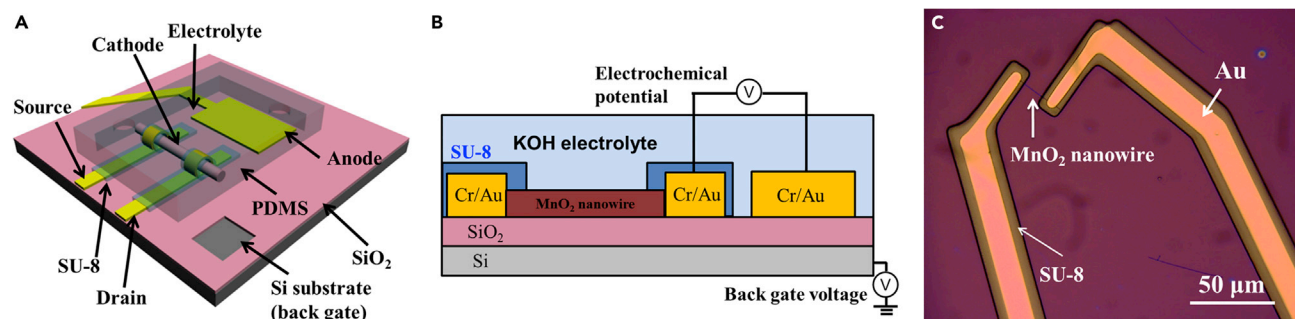


Figure 1. Configuration of the field-effect energy-storage device (FE-ESD)

(A and B) A three-dimensional view and a cross section of the FE-ESD based on a single α -MnO₂ nanowire.

(C) Optical image for the FE-ESD showing the α -MnO₂ nanowire in contact with two gold electrodes. SU-8 is used to cover the gold electrodes to prevent current leakage.

induced gate voltages. Thus, the overarching objective of the present paper is to determine whether such electric field effects can be used to influence and perhaps enhance the energy-storage properties of an electrochemical device.

To explore the question of whether EDOS influences energy storage, we have designed a nanowire-based, field-effect energy-storage device (FE-ESD; Figure 1A). The device is based on using a single manganese dioxide (α -MnO₂) nanowire of 30 nm in diameter and \sim 20 μ m in length. The detailed fabrication procedure is shown in Figure S1. From the electrochemical point of view, the α -MnO₂ nanowire functions as the cathode while the large gold pad as the anode, with an electrolyte of 6 mol/L KOH (potassium hydroxide). The configuration of our energy-storage device is similar to the on-chip electrochemical nanodevices reported previously, which has been demonstrated as a powerful tool in understanding the insight of electrochemical processes.^{20–24} In the “field-effect” part of the FE-ESD, an additional electrical potential (gate voltage) is induced via Si versus the ground. The highly doped Si substrate and the 300 nm SiO₂ layer serve as the back gate and dielectric layer, respectively (Figure 1B). The α -MnO₂ nanowire acts as a semiconductor channel in which the gate electrode is expected to influence the flow of charge. Thus, the FE-ESD integrates an electrochemical device structure with a gate electrode configuration, whereas the α -MnO₂ nanowire serves as both the cathode electrochemically and as a conductive channel “field-effect” wise. With this configuration, we are able to determine how the gate voltage influences the electrode/electrolyte interface and the resulting energy-storage behavior. The optical image (Figure 1C) shows that the α -MnO₂ nanowire is anchored by Au electrodes and that these electrodes are fully covered by an SU-8 passivation layer to avoid current leakage. We have tested the leakage currents of these nanowire devices from two sources, from the SiO₂ dielectric layer and from the current collector with the SU-8 passivation layer to the electrolyte. The first one was determined to be less than 0.15 nA under 1 V (Figure S2C). The second was characterized (Figure S2D) using a 3-electrode cell in which the α -MnO₂ was charged to 0.4 V versus saturated calomel electrode (SCE), and the self-discharge properties were measured. A leakage current of 5 pA was obtained.

RESULTS AND DISCUSSION

We have investigated the electrochemical performance of the FE-ESD at different gate voltages by using a probe station, an electrochemical workstation, and a semiconductor device analyzer. Cyclic voltammetry (CV) was used to characterize the

¹State Key Laboratory of Advanced Technology for Materials Synthesis and Processing, Wuhan University of Technology, Wuhan 430070, China

²Department of Materials Science and Engineering, University of Washington, Seattle, WA 98105, USA

³Department of Mechanical Engineering, The University of Melbourne, Melbourne, VIC 3010, Australia

⁴Department of Chemistry and Biochemistry, University of California, Los Angeles, Los Angeles, CA 90095, USA

⁵Foshan Xianhu Laboratory of the Advanced Energy Science and Technology Guangdong Laboratory, Xianhu hydrogen Valley, Foshan, Guangdong 528200, China

⁶Hubei Longzhong Laboratory, Xiangyang, Hubei 441000, China

⁷These authors contributed equally

⁸Lead contact

*Correspondence: mlq518@whut.edu.cn
<https://doi.org/10.1016/j.chempr.2022.05.004>

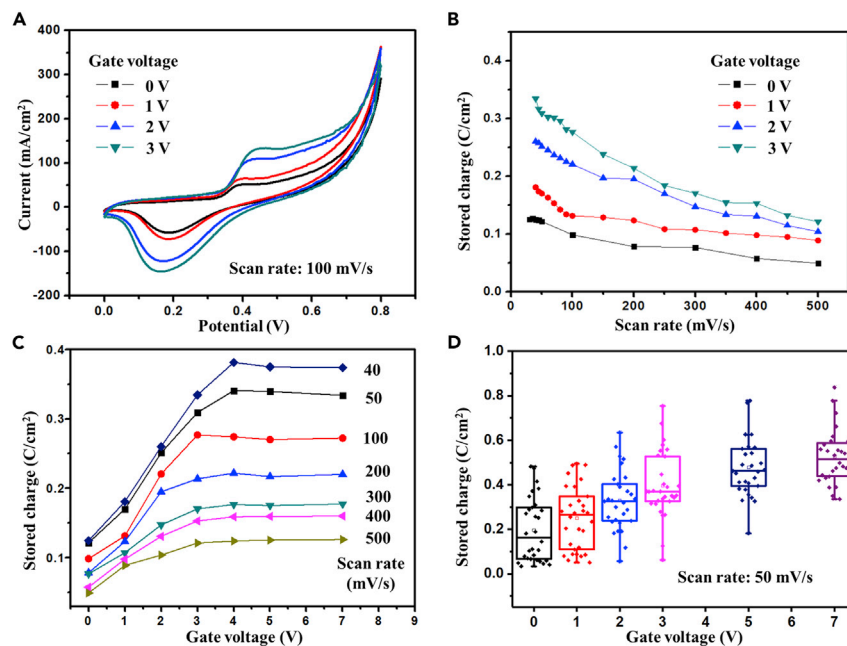


Figure 2. Electrochemical performance of the α -MnO₂ single-nanowire FE-ESD

(A) CV curves at 100 mV/s with the gate voltages of 0, 1, 2, and 3 V.

(B) The stored charge as a function of scan rate (30–500 mV/s).

(C) The stored charge as a function of the gate voltage (0–7 V).

(D) The stored charge for thirty-one devices as a function of the gate voltage at a scan rate of 50 mV/s. The highest and lowest horizontal lines in the boxes represent the upper and lower quartiles, respectively, whereas the middle line represents the mean.

energy-storage properties of devices. By comparing the CV of FE-ESDs with and without the α -MnO₂ (current flow through the α -MnO₂ and electrolyte, respectively), we are able to determine how much stored charge is attributable to the α -MnO₂ nanowire and the background. As shown in Figures S3 and S9, at a scan rate of 100 mV/s, the stored charge of the α -MnO₂ single-nanowire FE-ESD is almost 10⁵ times greater than that of the background. We subsequently applied the gate voltage to the α -MnO₂ FE-ESD to determine its influence on energy storage. Upon increasing the gate voltage from 0 to 3 V, the area under the CV curve at 100 mV/s is nearly tripled (Figure 2A). Specifically, the stored charge increases monotonically from \sim 100 mC/cm² at 0 V to 277 mC/cm² with a gate voltage of 3 V. The scan rate dependence of the stored charge as a function of the gate voltage is shown in Figure 2B. Even at a relatively high scan rate of 500 mV/s, the stored charge (120 mC/cm²) at 3 V is still 2.5 times greater. When further increasing the gate voltage from 3 to 4 V, the stored charge shows a moderate growth. Increasing the gate voltage beyond 4 V does not provide any additional benefit as the stored charge remains constant in the range between 4 and 7 V (Figures 2C and S4A).

We carried out two other series of experiments to verify the reproducibility of these gate-voltage results. In one case, 31 α -MnO₂ FE-ESDs were fabricated and tested at a scan rate of 50 mV/s. The data shown in Figure 2D indicate that although there are device-to-device variations, the stored charge at a gate voltage of 3 V is, on average, two times greater than that at 0 V. The stored charge variation among the devices is attributed to the different diameter, Fermi-level position, and carrier density of the MnO₂ nanowires. Specifically, a higher diameter of MnO₂ will lead to a higher stored charge per area. We also carried out electrochemical three-electrode measurements

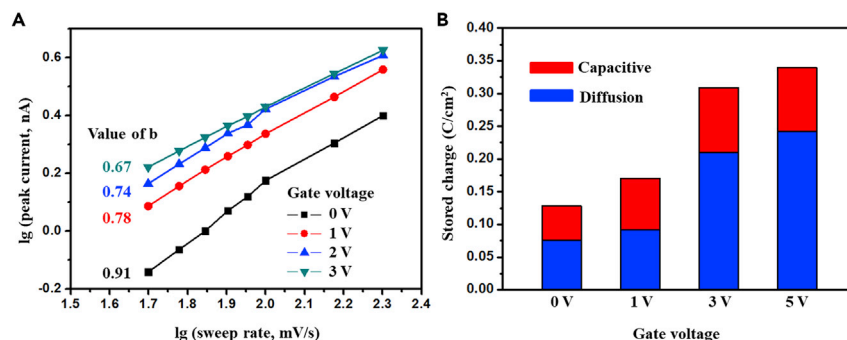


Figure 3. Kinetics of the α -MnO₂ single-nanowire FE-ESD electrochemical behavior

(A) A plot of $\log(i)$ versus $\log(v)$ for scan rates from 50 to 200 mV/s to determine b in Equation 1. (B) Bar chart showing the contributions of stored charge from capacitance and diffusion at a scan rate of 50 mV/s.

as a reference electrode (SCE) was integrated into the device structure shown in Figure 1. As shown in Figures S4B–S4D, a conclusion similar to that from the two-electrode experiment can be drawn with respect to the gate voltage and scan rate dependences. The three-electrode experiment (Figure S4B) also shows that oxidation and reduction peak occur at 0.18 and 0.02 V versus SCE, respectively. These peaks are attributed to the equilibrium potential of the Mn⁴⁺/Mn³⁺ redox.^{25–27}

Accompanying the stored charge increase with gate voltage is the increased voltage offset between oxidation and reduction peaks (Figure S5). Usually, an increase in polarization indicates a decrease in the ion/electron diffusion rate and poor electrochemical performance. In our study, however, the stored charge increases as the voltage separation increases. To discern the influence of the gate voltage, we studied the charge storage mechanism of the FE-ESD in greater detail. We assumed that the peak current (i) of the CV obeys a power-law relationship with the scan rate v

$$i = av^b, \quad (\text{Equation 1})$$

where a and b are adjustable values.^{28–30} The value of b provides an insight into the charge storage mechanism as to whether the currents are limited by semi-infinite diffusion ($b = 0.5$) or surface controlled ($b = 1$). Figure 3A shows a plot of $\log(i)$ of the cathodic peak versus $\log(v)$ at different gate voltages. For scan rates between 50 and 200 mV/s, b is 0.91 at a gate voltage of 0 V, indicating that the kinetics are surface controlled. This behavior is expected because of the α -MnO₂ nanowire geometry. As the gate voltage increases to 3 V, b decreases continuously from 0.91 to 0.67. This suggests that the redox reaction is not only occurring at the surface of the nanowire but, because of a greater diffusion contribution, also extending further into the nanowire.³¹ Thus, upon increasing the gate voltage, there is a greater amount of energy storage as the redox reactions are not confined to the surface but penetrate the 30 nm diameter wire.

We also use the CV results to quantify the stored charge associated with diffusion- and surface-controlled mechanisms. In this case, we use the relation

$$i(V) = a_1v + a_2v^{1/2}, \quad (\text{Equation 2})$$

where the current response (i) at a potential (V) can be described as a combination of two mechanisms, surface-controlled charge storage (a_1v) and diffusion-controlled one ($a_2v^{1/2}$).^{32,33} We then calculate the values of a_1 and a_2 over the potential range

(0–0.8 V) to obtain the amount of charge storage for each mechanism. At 50 mV/s, we find that the amount of stored charge associated with diffusion-controlled processes increases substantially from 0.076 C/cm² at 0 V to 0.242 C/cm² at 3 V. The increase in the surface-controlled contribution exhibits only a modest increase from 0.052 to 0.097 C/cm². This analysis shows that the surface-controlled currents remain relatively constant with the application of the gate voltage but that the diffusion-controlled currents are largely responsible for the energy-storage increase.

We further employed the open-circuit potential (OCP) to reveal the gate-voltage-dependent Fermi level of α -MnO₂ in the electrolyte. These Fermi-level positions, subsequently, were applied to the electronic band structures to understand the effects of the gate voltage on the energy-storage device performance. As shown in Figure 4A, the OCP of α -MnO₂ is –0.25 V versus SCE when the gate voltage is 0 V (equal to 4.38 eV versus vacuum). When the gate voltage is increased to 3 V, the electrons are injected into the bottom surface area of α -MnO₂ (Figures 4B and 4C3 area), leading to a lower OCP of –1.70 V versus SCE (Figure 4A), corresponding to a higher Fermi level of 2.98 eV. Meanwhile, the Fermi level in the α -MnO₂ upper-surface area remains unchanged (Figures 4B and 4C1 area).

To fully understand the band bending at the MnO₂-electrolyte interface, as well as how this influences the redox reaction, two parameters are introduced into the band diagram. (1) The first one is the Fermi level in the 6 M KOH aqueous solution ($E_{\text{H}_2\text{O}/\text{H}^+}$), which is $\Phi_{\text{SHE}} - 0.059 \times \text{pH} = 3.57$ eV (Figure 4C). When the MnO₂-electrolyte interface forms, the Fermi level of the MnO₂ is aligned to that of the electrolyte. At the C3 area, the Fermi level of MnO₂ located at 2.98 eV is smaller than 3.57 eV, resulting in an upward band bending (Figure 4C3). Reversely, a downward band bending forms at the C1 area due to the larger Fermi level of 4.38 eV (Figure 4C1). (2) The other is the H⁺ redox potential in α -MnO₂. In the band diagram, the incorporated ions are treated as the extrinsic impurities, which occupy certain electronic energy levels within the α -MnO₂ band gap. The H⁺ insertion level, located at 4.84 eV (in 6 M KOH electrolyte), is calculated according to the study conducted by³⁴ and shown in Figure 4C.

In an electrochemical system, its electrochemical reaction should take place while the scanned potential windows by the electrolytes ($e\Phi$) pass through the H⁺ insertion level as shown in Figure 4C. When there is no gate voltage, the electrochemical reaction should take place near $e\Phi = 4.84$ eV. This value is reasonably consistent with our experimental result shown in Figure S4B, $e\Phi = 4.80$ eV (0.12 V versus SCE). The 0.04 eV difference contributes to the downward band bending at the α -MnO₂-electrolyte interface (Figure 4C1). As indicated in Figure 3A, the redox reactions are confined to the surface of the α -MnO₂ nanowire. Thus, the redox potential is only slightly influenced by the band bending, decreasing from 4.84 to 4.80 eV. Upon increasing the gate voltage, the Fermi level of α -MnO₂ moves from 4.38 to 2.98 eV, resulting in an upward band bending (Figure 4C3). Therefore, higher redox potential is observed in Figure 2A (Figures S10 and S11).

Besides the higher redox potential, other two interesting phenomena emerged by applying the back-gate voltages, the broader redox peaks and the greater stored charge (Figure 2A). These two experimental results are explained in Figures 4D and 4E. With the gate voltage, the energy state of the α -MnO₂ bottom surface is schematically shown in Figure 4C3, whereas its top surface stays at the original state (shown in Figure 4C1). Hence, there is a Fermi-level gradient in the α -MnO₂ nanowire along with the electric field direction. In the middle, there exists a point with no band

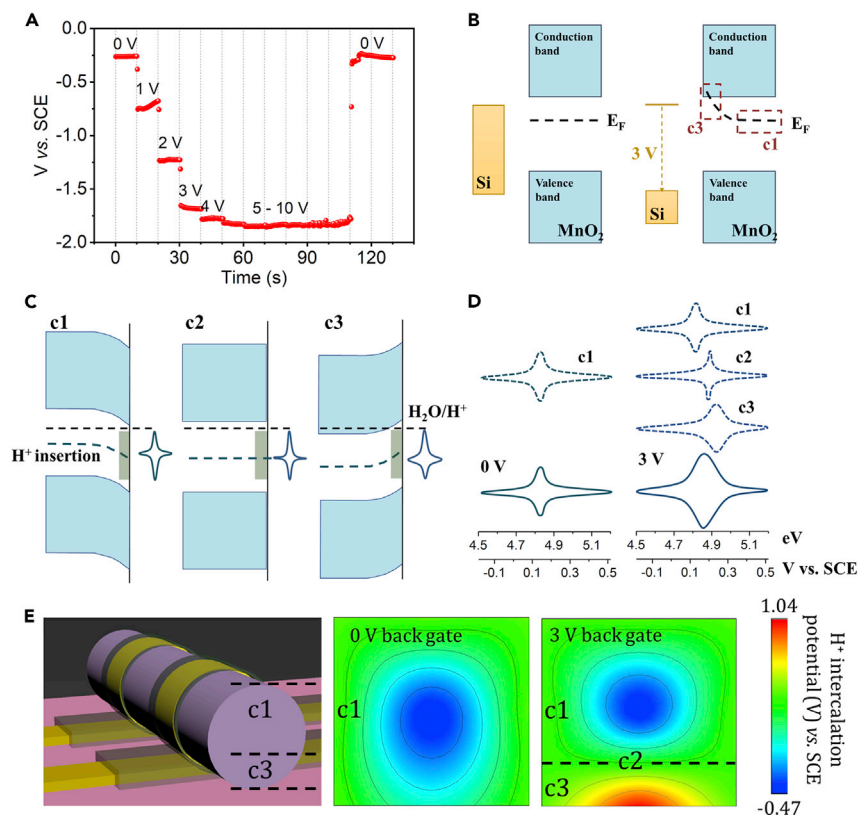


Figure 4. Gate-voltage-dependent open-circuit potential and band diagram of α -MnO₂ immersed in a 6 M KOH aqueous solution.

(A) Gate-voltage induced open-circuit potential changes in a 6 M KOH.

(B) (Left) The band structure of the device without back-gate voltage. (Right) The applied 3 V gate voltage will move the conduction band, valence band, the Fermi level, and H⁺ energy level downward before the α -MnO₂ nanowire touching the electrolyte.

(C) (C1) The non-gate-controlled area, including the case without gate voltage and the upper area of α -MnO₂ at 3 V back-gate voltage, will bend down. (C2) A specific state in which no band bending occurs. This phenomenon will likely appear in the middle part of α -MnO₂ at 3 V back-gate voltage. (C3) Opposite to the non-gate-controlled area shown in Figure 4C1, the bottom area of α -MnO₂ bends up when in touch with the electrolyte.

(D) The simulated CV curve without back-gate voltage and at 3 V back-gate voltage. The band bending as shown in Figures 4C1–4C3 leads to different CV curves. The reaction potential at 3 V back-gate voltage contains all situations shown in Figures 4C1, 4C2, and 4C3, resulting in broader redox peaks and upper-shift redox potential.

(E) The schematics of H⁺ insertion potential in MnO₂. Under zero back-gate voltage, only the C1 state exists in MnO₂. For 3 V back-gate voltage, the higher H⁺ insertion potential area emerges (C3), resulting in the higher redox potential.

bending (Figure 4C2). The Fermi-level gradient increases the accessible EDOS participating in the reaction. As a result, the CV at 3 V gate voltage contains all of the three situations in Figures 4C1, 4C2, and 4C3. The reaction potential range (E) at 3 V gate voltage is broader than that without gate voltage, leading to the widening of redox peaks (Figures 4C and 4D). The H⁺ insertion potential in MnO₂ is schematically shown in Figure 4E. A red (high potential) region forms after applying the gate voltage, leading to a higher average redox potential of the MnO₂ and the broadened redox peaks. Furthermore, for a CV experiment, there is $t = E/v$ in which t is the reaction time for a specific redox reaction, E is the potential range of the redox reaction, and v is the scan rate. After applying the gate voltage, a

broader reaction potential range E is obtained. At a specific scan rate v , the reaction time t will be longer, and thus more ions participate in the reaction.

The interesting back-gate-enhanced charge storage in MnO_2 nanowire is not limited to the liquid electrolyte. A similar phenomenon is observed with a solid electrolyte and with varying insulating layer thicknesses (Figure S6). In addition to the results for $\alpha\text{-MnO}_2$, comparable experiments carried out using molybdenum disulfide (MoS_2) nanosheets show that the application of a gate voltage leads to enhanced energy storage (Figure S7). Interestingly, graphite sheets show no improvement in charge storage, even at a high gate voltage of 10 V (Figure S8). The reason for this is that the principal charge storage mechanism for graphene sheets, the electrochemical double-layer capacitance, has a minimal contribution from the redox reactions.

Conclusions

Our study shows that by modifying the configuration of a nanowire electrochemical cell to include a gate electrode, it is possible to increase the energy-storage properties of the device. Analysis of the CV experiment shows that without the gate voltage, redox reactions are confined to the surface of the $\alpha\text{-MnO}_2$ nanowire and that by increasing the gate voltage, redox reactions extend beyond the nanowire surface and lead to the energy-storage increase. The energy band diagram semi-quantitatively shows that the proton insertion energy level bending under gate voltage contributes to the higher redox potential, quadrupled energy storage, and the broader redox peaks. Finally, the initial results for MoS_2 suggest that the gate-voltage-induced increase in energy storage may be applicable to many other redox-active materials.

EXPERIMENTAL PROCEDURES

Resource availability

Lead contact

Further information and requests for resources should be directed to and will be fulfilled by the lead contact, Liqiang Mai (mlq518@whut.edu.cn).

Materials availability

This study did not generate new unique materials.

Data and code availability

The datasets supporting this study are available from the [lead contact](#) upon request.

Experimental methods

Synthesis of MnO_2 nanowires

The $\alpha\text{-MnO}_2$ nanowires were synthesized by a hydrothermal method following a previous report.³⁵ In a typical synthesis, 2 mmol of KMnO_4 and 2 mmol of NH_4F can be dissolved in 80 mL of water and stirred at 25°C for 1 h. The solution is then poured into a 100 mL autoclave and heated at 180°C for 48 h. After washing and drying, the $\alpha\text{-MnO}_2$ nanowires, which are over 20 μm in length and 20–40 nm in diameter, are obtained. The large length and small diameter of our synthesized $\alpha\text{-MnO}_2$ nanowires make it possible to fabricate single-nanowire-based energy-storage devices.

Device fabrication and characterization

A Cr/Au (5/50 nm) counter electrode was first deposited onto a silicon wafer with a 300 nm thick layer of SiO_2 using the electron-beam lithography followed by physical vapor deposition and lift off. The $\alpha\text{-MnO}_2$ nanowire was immobilized by the Cr/Au (5/150 nm) contact and a SU-8 passivation layer deposition. Finally, electrolyte

(6 mol/L KOH) was used to cover the working electrode (α -MnO₂ nanowire) and counter electrode (Cr/Au pad) of the energy-storage device. CV of the field-effect-modulated energy-storage device and the rate behavior at different gate voltages were measured using a probe station (Lake Shore PPT4), an electrochemical workstation (Autolab PGSTAT 302N), and a semiconductor device analyzer (Agilent B1500A).

SUPPLEMENTAL INFORMATION

Supplemental information can be found online at <https://doi.org/10.1016/j.chempr.2022.05.004>

ACKNOWLEDGMENTS

This work was supported by the National Key Research and Development Program of China (2020YFA0715000 and 2016YFA0202603), the National Natural Science Foundation of China (52127816, 51832004, 51872218, and 51521001), the Fundamental Research Funds for the Central Universities (WUT: 2022IVA007 and 2022IV015h), and the Foshan Xianhu Laboratory of the Advanced Energy Science and Technology Guangdong Laboratory (XHT2020-003).

AUTHOR CONTRIBUTIONS

Conceptualization, L.M. and M.Y.; methodology, M.Y.; investigation, M.Y., P.W., X.P., C.H., Q.W., and Y.Z.; formal analysis, L.M., M.Y., P.W., J.Z.L., C.H., Y.Z., J.Y., and B.D.; writing –original draft, M.Y.; writing – review & editing, L.M., M.Y., P.W., X.P., J.Z.L., C.H., K.Z., Y.Z., Q.W., J.Y., and B.D.; supervision, L.M.

DECLARATION OF INTERESTS

The authors declare no competing interests.

Received: November 7, 2021

Revised: December 16, 2021

Accepted: May 10, 2022

Published: June 2, 2022

REFERENCES

- Hochbaum, A.I., Chen, R., Delgado, R.D., Liang, W., Garnett, E.C., Najarian, M., Majumdar, A., and Yang, P. (2008). Enhanced thermoelectric performance of rough silicon nanowires. *Nature* 451, 163–167. <https://doi.org/10.1038/nature06381>.
- Wu, W., Wang, L., Li, Y., Zhang, F., Lin, L., Niu, S., Chenet, D., Zhang, X., Hao, Y., Heinz, T.F., et al. (2014). Piezoelectricity of single-atomic-layer MoS₂ for energy conversion and piezotronics. *Nature* 514, 470–474. <https://doi.org/10.1038/nature13792>.
- Jiang, Z., Qing, Q., Xie, P., Gao, R., and Lieber, C.M. (2012). Kinked p-n junction nanowire probes for high spatial resolution sensing and intracellular recording. *Nano Lett.* 12, 1711–1716. <https://doi.org/10.1021/nl300256r>.
- Duan, X., Gao, R., Xie, P., Cohen-Karni, T., Qing, Q., Choe, H.S., Tian, B., Jiang, X., and Lieber, C.M. (2011). Intracellular recordings of action potentials by an extracellular nanoscale field-effect transistor. *Nat. Nanotechnol.* 7, 174–179. <https://doi.org/10.1038/nnano.2011.223>.
- Kucsko, G., Maurer, P.C., Yao, N.Y., Kubo, M., Noh, H.J., Lo, P.K., Park, H., and Lukin, M.D. (2013). Nanometre-scale thermometry in a living cell. *Nature* 500, 54–58. <https://doi.org/10.1038/nature12373>.
- Huang, Y., Duan, X., Wei, Q., and Lieber, C.M. (2001). Directed assembly of one-dimensional nanostructures into functional networks. *Science* 291, 630–633. <https://doi.org/10.1126/science.291.5504.630>.
- Novoselov, K.S., Geim, A.K., Morozov, S.V., Jiang, D., Zhang, Y., Dubonos, S.V., Grigorieva, I.V., and Firsov, A.A. (2004). Electric field effect in atomically thin carbon films. *Science* 306, 666–669. <https://doi.org/10.1126/science.1102896>.
- Radisavljevic, B., Radenovic, A., Brivio, J., Giacometti, V., and Kis, A. (2011). Single-layer MoS₂ transistors. *Nat. Nanotechnol.* 6, 147–150. <https://doi.org/10.1038/nnano.2010.279>.
- Britnell, L., Gorbachev, R.V., Jalil, R., Belle, B.D., Schedin, F., Mishchenko, A., Georgiou, T., Katsnelson, M.I., Eaves, L., Morozov, S.V., et al. (2012). Field-effect tunneling transistor based on vertical graphene heterostructures. *Science* 335, 947–950. <https://doi.org/10.1126/science.1218461>.
- Huang, Y., Duan, X., Cui, Y., Lauhon, L.J., Kim, K.-H., and Lieber, C.M. (2001). Logic gates and computation from assembled nanowire building blocks. *Science* 294, 1313–1317. <https://doi.org/10.1126/science.1066192>.
- Dhoot, A.S., Yuen, J.D., Heeney, M., McCulloch, I., Moses, D., and Heeger, A.J. (2006). Beyond the metal-insulator transition in polymer electrolyte gated polymer field-effect transistors. *Proc. Natl. Acad. Sci. USA* 103, 11834–11837. <https://doi.org/10.1073/pnas.0605033103>.
- Dhoot, A.S., Israel, C., Moya, X., Mathur, N.D., and Friend, R.H. (2009). Large electric field effect in electrolyte-gated manganites. *Phys. Rev. Lett.* 102, 136402. <https://doi.org/10.1103/PhysRevLett.102.136402>.

13. Ye, J.T., Inoue, S., Kobayashi, K., Kasahara, Y., Yuan, H.T., Shimotani, H., and Iwasa, Y. (2010). Liquid-gated interface superconductivity on an atomically flat film. *Nat. Mater.* **9**, 125–128. <https://doi.org/10.1038/nmat2587>.
14. Bollinger, A.T., Dubuis, G., Yoon, J., Pavuna, D., Misewich, J., and Božović, I. (2011). Superconductor-insulator transition in $\text{La}_{2-x}\text{Sr}_x\text{CuO}_4$ at the pair quantum resistance. *Nature* **472**, 458–460. <https://doi.org/10.1038/nature09998>.
15. Zhu, J., Chen, M., Wei, H., Yerra, N., Haldolaarachchige, N., Luo, Z., Young, D.P., Ho, T.C., Wei, S., and Guo, Z. (2014). Magnetocapacitance in magnetic microtubular carbon nanocomposites under external magnetic field. *Nano Energy* **6**, 180–192. <https://doi.org/10.1016/j.nanoen.2014.04.002>.
16. Wei, H., Gu, H., Guo, J., Wei, S., Liu, J., and Guo, Z. (2013). Silica doped polyaniline with endured electrochemical energy storage and the magnetic field effects. *J. Phys. Chem. C* **117**, 13000–13010. <https://doi.org/10.1021/jp403656q>.
17. Zhu, J., Chen, M., Qu, H., Luo, Z., Wu, S., Colorado, H.A., Wei, S., and Guo, Z. (2013). Magnetic field induced capacitance enhancement in graphene and magnetic graphene nanocomposites. *Energy Environ. Sci.* **6**, 194–204. <https://doi.org/10.1039/C2EE23422J>.
18. Tataru, R., Karayalali, P., Yu, Y., Zhang, Y., Giordano, L., Maglia, F., Jung, R., Schmidt, J.P., Lund, I., and Shao-Horn, Y. (2019). The effect of electrode-electrolyte interface on the electrochemical impedance spectra for positive electrode in Li-ion battery. *J. Electrochem. Soc.* **166**, A5090–A5098. <https://doi.org/10.1149/2.0121903jes>.
19. Liu, X., Li, B., Li, X., Harutyunyan, A.R., Hone, J., and Esposito, D.V. (2019). The critical role of electrolyte gating on the hydrogen evolution performance of monolayer MoS_2 . *Nano Lett.* **19**, 8118–8124. <https://doi.org/10.1021/acs.nanolett.9b03337>.
20. Wang, P., Yan, M., Meng, J., Jiang, G., Qu, L., Pan, X., Liu, J.Z., and Mai, L. (2017). Oxygen evolution reaction dynamics monitored by an individual nanosheet-based electronic circuit. *Nat. Commun.* **8**, 645. <https://doi.org/10.1038/s41467-017-00778-z>.
21. Yang, H., He, Q., Liu, Y., Li, H., Zhang, H., and Zhai, T. (2020). On-chip electrocatalytic microdevice: an emerging platform for expanding the insight into electrochemical processes. *Chem. Soc. Rev.* **49**, 2916–2936. <https://doi.org/10.1039/C9CS00601J>.
22. Yan, M., Pan, X., Wang, P., Chen, F., He, L., Jiang, G., et al. (2017). Field-effect tuned adsorption dynamics of VSe_2 nanosheets for enhanced hydrogen evolution reaction. *Nano Lett.* **17**, 4109–4115. <https://doi.org/10.1021/acs.nanolett.7b00855>.
23. Pan, X., Hong, X., Xu, L., Li, Y., Yan, M., and Mai, L. (2019). On-chip micro/nano devices for energy conversion and storage. *Nano Today* **28**, 100764. <https://doi.org/10.1016/j.nantod.2019.100764>.
24. He, Y., He, Q., Wang, L., Zhu, C., Golani, P., Handoko, A.D., Yu, X., Gao, C., Ding, M., Wang, X., et al. (2019). Self-gating in semiconductor electrocatalysis. *Nat. Mater.* **18**, 1098–1104. <https://doi.org/10.1038/s41563-019-0426-0>.
25. Kozawa, A., and Powers, R.A. (1966). The manganese dioxide electrode in alkaline electrolyte; the electron-proton mechanism for the discharge process from MnO_2 to $\text{MnO}_{1.5}$. *J. Electrochem. Soc.* **113**, 870–878. <https://doi.org/10.1149/1.2424145>.
26. Qu, D.Y., Conway, B.E., Bai, L., Zhou, Y.H., and Adams, W.A. (1993). Role of dissolution of Mn (iii) species in discharge and recharge of chemically-modified MnO_2 battery cathode materials. *J. Appl. Electrochem.* **23**, 693–706. <https://doi.org/10.1007/BF00243339>.
27. Fiedler, D.A. (1998). Rapid evaluation of the rechargeability of c- MnO_2 in alkaline media by abrasive stripping voltammetry. *J. Solid State Electrochem.* **2**, 315–320. <https://doi.org/10.1007/s100080050106>.
28. Lindström, H., Södergren, S., Solbrand, A., Rensmo, H., Hjelm, J., Hagfeldt, A., and Lindquist, S.-E. (1997). Li^+ ion insertion in TiO_2 (anatase). 2. Voltammetry on nanoporous films. *J. Phys. Chem. B* **101**, 7717–7722. <https://doi.org/10.1021/jp970490q>.
29. Choi, C., Ashby, D.S., Butts, D.M., DeBlock, R.H., Wei, Q., Lau, J., and Dunn, B. (2020). Achieving high energy density and high power density with pseudocapacitive materials. *Nat. Rev. Mater.* **5**, 5–19. <https://doi.org/10.1038/s41578-019-0142-z>.
30. Xiong, F., Jiang, Y., Cheng, L., Yu, R., Tan, S., Tang, C., Zuo, C., An, Q., Zhao, Y., Gaumet, J.J., and Mai, L. (2022). Low-strain TiP_2O_7 with three-dimensional ion channels as long-life and high-rate anode material for Mg-ion batteries. *Interdiscip. Mater.* **1**, 140–147. <https://doi.org/10.1002/idm2.12004>.
31. Brezesinski, T., Wang, J., Tolbert, S.H., and Dunn, B. (2010). Ordered mesoporous $\alpha\text{-MoO}_3$ with iso-oriented nanocrystalline walls for thin-film pseudocapacitors. *Nat. Mater.* **9**, 146–151. <https://doi.org/10.1038/nmat2612>.
32. Wang, J., Polleux, J., Lim, J., and Dunn, B. (2007). Pseudocapacitive contributions to electrochemical energy storage in TiO_2 (anatase) nanoparticles. *J. Phys. Chem. C* **111**, 14925–14931. <https://doi.org/10.1021/jp074464w>.
33. Sathya, M., Prakash, A.S., Ramesha, K., Tarascon, J.M., and Shukla, A.K. (2011). V_2O_5 -anchored carbon nanotubes for enhanced electrochemical energy storage. *J. Am. Chem. Soc.* **133**, 16291–16299. <https://doi.org/10.1021/ja207285b>.
34. Young, M.J., Holder, A.M., George, S.M., and Musgrave, C.B. (2015). Charge storage in cation incorporated $\alpha\text{-MnO}_2$. *Chem. Mater.* **27**, 1172–1180. <https://doi.org/10.1021/cm503544e>.
35. Hu, P., Yan, M., Wang, X., Han, C., He, L., Wei, X., Niu, C., Zhao, K., Tian, X., Wei, Q., et al. (2016). Single-nanowire electrochemical probe detection for internally optimized mechanism of porous graphene in electrochemical devices. *Nano Lett.* **16**, 1523–1529. <https://doi.org/10.1021/acs.nanolett.5b03576>.